Algorithm Theoretical Basis Document: Sea Ice Products: Updated December 2011

Thorsten Markus, Donald J. Cavalieri and
Alvaro Ivanoff
Cryospheric Sciences Laboratory
NASA Goddard Space Flight Center
Greenbelt, MD 20771

1. Overview

The AMSR-E sea ice standard level 3 products include sea ice concentration, snow depth on sea ice, and sea ice drift. The AMSR-E standard sea ice concentration product is generated using the enhanced NASA Team (NT2) algorithm described by Markus and Cavalieri (2000, 2009), the snow depth is produced from the algorithm described by Markus and Cavalieri (1998) for both hemispheres, but excluding the Arctic perennial ice regions, and the sea ice drift is produced from an algorithm described by (Liu and Cavalieri 1998). Additionally, the difference between the AMSR-E Bootstrap (ABA) (see ATBD by J.C. Comiso) and the NT2 retrieved concentrations (ABA-NT2) are archived. These products together with AMSR-E calibrated brightness temperatures (TBs) are mapped to the same polar stereographic projection used for SSM/I data to provide the research community consistency and continuity with the existing 32-year Nimbus 7 SMMR and DMSP SSM/I sea ice concentration products. The TB grid resolutions are as follows: (a) TBs for all AMSR-E channels: 25-km, (b) TBs for the 18, 23, 36, and 89 GHz channels: 12.5-km, (c) TBs for the 89 GHz channels: 6.25-km. All of these TB products are stored as a composite of (i) daily-averaged ascending orbits only, (ii) daily-averaged descending orbits only, and (iii) all orbits creating a full daily average. Sea ice concentrations are produced at 12.5-km and 25-km resolutions and stored as a composite of daily-averaged ascending orbits, daily-averaged descending orbits, and all orbits for a full daily average, similar to the TB products. (e) Snow depth on sea ice is produced as a 5-day average at a resolution of 12.5 km. Sea ice drift is also a five-day product computed at a resolution of 6.25-km, but mapped at a resolution of 100-km.

2. Sea Ice Concentration

2.1 Algorithm Theoretical Basis

The two ratios of brightness temperatures used in the original NASA Team algorithm (Cavalieri et al., 1984; Gloersen and Cavalieri, 1986; Cavalieri et al., 1995) as well as in the NT2 approach are the polarization

$$PR(\nu) = [TB(\nu V) - TB(\nu)] / [TB(\nu V) + TB(\nu H)]$$

and the spectral gradient ratio

$$GR(\nu 1p\nu 2p) = TB(\nu 1p) - TB(\nu 2p)] / [TB(\nu 1p) + TB(\nu 2p)]$$

where TB is the brightness temperature at frequency ν for the polarized component p (vertical (V) or horizontal (H)).

Figure 1(top) shows a typical scatterplot of PR(19) versus GR(37V19V) for September conditions in the Weddell Sea. The NT algorithm identifies two ice types which are associated with first-year and multiyear ice in the Arctic and ice types A and B in the Antarctic (as shown in Figure 1(top)). The A-B line represents 100% ice concentration. The distance from the open water point (OW) to line A-B is a measure of the ice concentration. In this algorithm, the primary source of error is attributed to conditions in the surface layer such as surface glaze and layering [Comiso et al., 1997], which can significantly affect the horizontally polarized 19 GHz brightness temperature [Matzler et al., 1984] leading to increased PR(19) values and thus an underestimate of ice concentration. In the following discussion, we will refer to these effects as surface effects. In Figure 1(top), pixels with significant surface effects tend to cluster as a cloud of points (labeled C) away from the 100% ice concentration line A-B resulting in an underestimate of ice concentration by the NT algorithm. The use of horizontally polarized channels makes it imperative to resolve a third ice type to overcome the difficulty of surface effects on the emissivity of the horizontally polarized component of the brightness temperature.

We make use of GR(89V19V) and GR(89H19H) to resolve the ambiguity between pixels with true low ice concentration and pixels with significant surface effects. A plot of these two ratios are found to form narrow clusters except for areas where surface effects decrease TB(19H) and consequently increase GR(89H19H) (Figure 1(bottom)). Values of high GR(89V19V) and high GR(89H19H) are indicative of open water. The range of GR(89H19H) values is larger because of the greater dynamic range between ice and water for the horizontally polarized components. With increasing ice concentration, the two ratios have more similar values. The narrow cluster of pixels adjacent to the diagonal shown in Figure 1(bottom) represents 100% ice concentration with different GR values corresponding to different ice types. When surface effects come into play, points deviate from this narrow cluster towards increased GR(89H19H) values (cloud of points to the right of the diagonal) while GR(89V19V) changes little or remains constant. This cloud of points labeled C in Figure 1(bottom) also corresponds to the cluster of points labeled C in Figure 1(top). The difference, therefore, between these two GRs (ΔGR) is used as a measure of the magnitude of surface effects. Based on this analysis we introduce a new ice type C which represents ice having significant surface effects. For computational reasons we rotate the axes in PR-GR space (Figure 1(top)) by an angle φ so the A-B line is vertical. This makes the rotated PRs ($PR_R(19)$ and $PR_R(89)$) independent of ice types A and B (first-year and multiyear for the Arctic). The use of the 89 GHz data requires a correction for atmospheric effects. This is accomplished through an additional AMSR-E variable, PR(89).

The response of the brightness temperatures to different weather conditions is calculated using an atmospheric radiative transfer model (Kummerow, 1993). Input data into the model are the emissivities of first-year sea ice under winter conditions taken from Eppler et al. (1992) with modifications to achieve agreement between modeled and observed ratios. Atmospheric profiles used as another independent variable in the algorithm, having different cloud properties, specifically cloud base, cloud top, cloud liquid water are taken from Fraser et al. (1975) and average atmospheric temperatures and humidity profiles for summer and winter conditions are taken from Antarctic research stations. These atmospheric profiles are based on climatology and are assumed valid for both hemispheres.

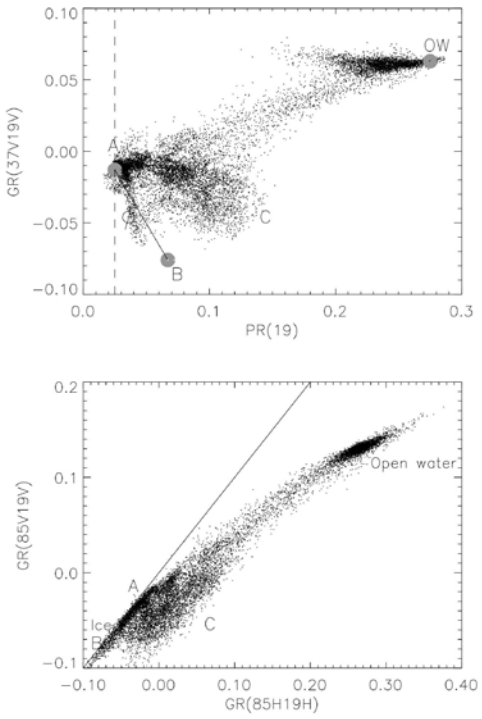

Figure 1 Top: GR(37V 19V) versus PR(19) for the Weddell Sea on September 15, 1992. The gray circles represent the tiepoints for the ice types A and B as well as for open water as used by the NT algorithm. Label C indicates pixels with significant surface effects. Φ is the angle between the y-axis and the A-B line. Bottom: GR(85V 19V) versus GR(85H19H). The ice types A and B are close to the diagonal. The amount of layering corresponds to the horizontal deviation from this line towards label C. Taken from Markus and Cavalieri [2000].

The plots of ΔGR versus PR_R (19) (Figure 2a) and ΔGR versus PR_R(89) (Figure 2b) illustrate the algorithm domain. The gray symbols indicate the tie-points with the different atmospheres for the three surface types (A, C, and OW). They also illustrate that the effect of weather is well modeled. For example, the cluster of open water values is mainly the result of changing atmospheric conditions. The modeled atmospheres adequately span the lengths of the OW clusters. A comparison of Figures 2a and 2b also

shows how much more the 89 GHz data are affected by the atmosphere compared to the 19 GHz data.

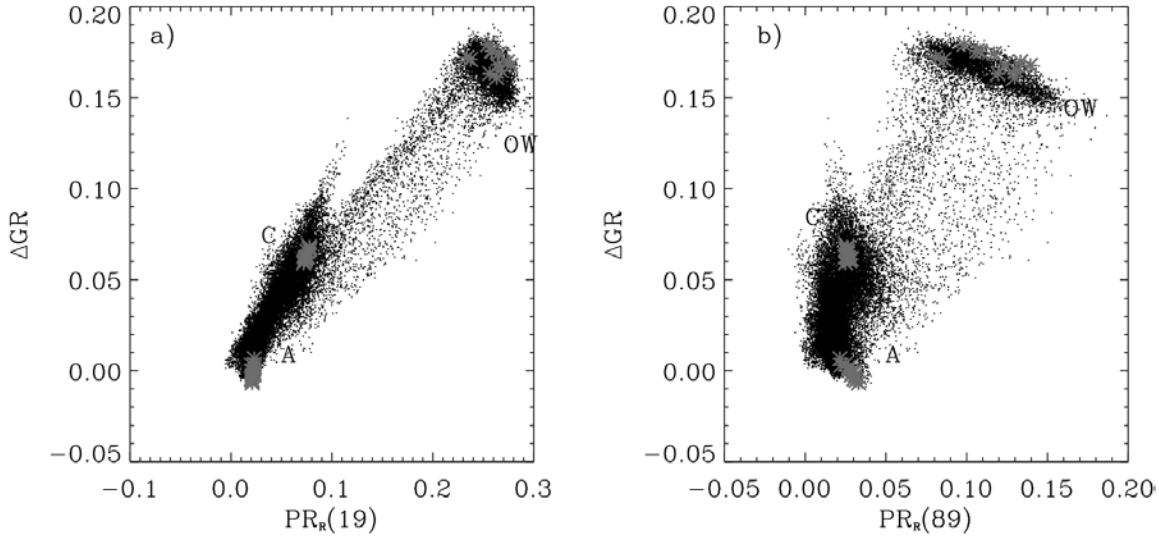

Figure 2 (a) ΔGR versus PR_R (19) and (b) ΔGR versus PR_R(89) for September 15, 2008. The gray symbols represent the NT2 tie-points.

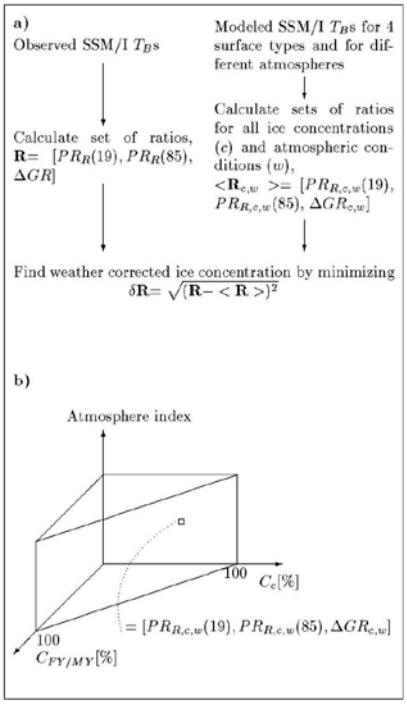

Figure 3. Flow diagram of the NT2 algorithm (from Markus and Dokken, 2002).

We, then, calculate brightness temperatures for all possible ice concentration combinations in 1% increments and for each of those solutions calculate the ratios PR_R (19), PR_R (89), and ΔGR. This creates a prism in which each element contains a vector

with the three ratios (Figure 3). For each AMSR-E pixel PR_R (19), PR_R (89), and ΔGR are calculated from the observed brightness temperatures. Next, we move through this prism comparing the observed three ratios with the modeled ones. The indices where the differences are smallest will determine the final ice concentration combination and weather index. The next section will provide detailed information about the implementation.

Because of the unique signature of new ice in the microwave range, we solve for new ice instead of ice type C for selected pixels. Using a GR(37V19V) threshold of –0.02 we either resolve ice type C (for pixels where GR(37V19V) is below this threshold) or thin ice (for pixels where GR(37V19V) is above this threshold). Areas of ice type C and thin ice are mutually exclusive because thin ice has little, if any, snow cover. A limitation, of course, is that we cannot resolve mixtures of thin ice and thicker ice with layering in its snow cover.

2.2 Implementation

2.2.1 Calculation of ice concentrations

In contrast to other operational sea ice concentration algorithms using daily averaged brightness temperatures as input, the AMSR-E NT2 concentrations are calculated from individual swath (Level 2) data from which daily maps are made by averaging these swath ice concentrations. Using swath brightness temperatures is particularly critical for the NT2 algorithm and its atmospheric correction. The atmospheric influence on the brightness temperatures is non linear and by using average brightness temperatures we would dilute the atmospheric signal. The ice concentration algorithm is implemented as follows:

1. Generate look-up tables: For each AMSR channel with frequency ν and polarization p calculate brightness temperature for each ice concentration-weather combination (using TBow, $TB_{A/FY}$, $TB_{C/thin}$ as given in the Appendix of Markus and Cavalieri (2009)):

$$TBca,cc,wx(\nu\, p) = (1 - C_A - C_C) \times TBow(\nu pWx) + C_A \times TB_{A/FY}(\nu pWx) + C_C \times TB_{C/thin}(\nu pWx) \quad (3)$$

where C_A refers to the ice type A/B concentration (FY/MY for Arctic), C_C to ice type C concentration, and Wx to the weather index. Ice concentrations are between 0 and 100 in 1% increments, weather indices are between 1 and 12 corresponding to the tables in the Appendix of Markus and Cavalieri (2009).

2. From these TBs calculate ratios creating the look-up tables, e.g. LUT $_{PR19(CA,CC,Wx)}$ etc.:

$$LUT_{PR19(CA,CC,Wx)} = [TBca,cc,wx(37V) - TBca,cc,wx(19V)] \text{ x } \sin\varphi_{19} / [TBca,cc,wx(37V) + TBca,cc,wx(19V)] + [TBca,cc,wx(19V) - TBca,cc,wx(19H)] \text{ x } \cos\varphi_{19}/$$

$$[TBca,cc,wx(19V) + TBca,cc,wx(19H)] \quad (4)$$

$$LUT_{PR89(ca,\ cc,wx)} = [TBca,cc,wx(37V) - TBca,cc,wx(19V)] \times \sin\varphi_{89}$$
$$TBca,cc,wx(37V) + TBca,cc,wx(19V)$$
$$+$$
$$[TBca,cc,wx(89V) - TBca,cc,wx(89H)] \times \cos\varphi_{89}/$$
$$[TBca,cc,wx(89V) + TBca,cc,wx(89H)] \quad (5)$$

If $GR(37V19V) \leq -0.02$ we solve for ice type C using ΔGR as our third variable, i.e.,

$$LUT_{dGR(ca,\ cc,wx)} = [TBca,cc,wx(89H) - TBca,cc,wx(19H)]/$$
$$[TBca,cc,wx(89H) + TBca,cc,wx(19H)]$$
$$-$$
$$[TBca,cc,wx(89V) - TBca,cc,wx(19V)]/$$
$$[TBca,cc,wx(89V) + TBca,cc,wx(19V)] \quad (6)$$

Whereas for pixels where $GR(37V19V) > -0.02$ we solve for thin ice using the standard GR(37V19V) as suggested by Cavalieri (1994), i.e.,

$$LUT_{dGR(ca,\ cc,wx)} = [TBca,cc,wx(37V) - TBca,cc,wx(19V)]/$$
$$[TBca,cc,wx(37V) + TBca,cc,wx(19V)] \quad (7)$$

Each of these arrays has the dimensions of 101 × 101 × 12 where, of course, the total ice concentration (ca + cc) cannot exceed 100.

3. For each pixel i we have the actual measured AMSR-E brightness temperatures (TBi(νp))

4. Calculate same ratios from these brightness temperatures as in step 2 (PRi(19), etc.).

5. Compare these observed ratios with each of the ratios in the look-up tables looping through all ice concentration-weather combinations, i.e.,

$$\delta = (PRi(19) - LUT_{PR19(ca,\ cc,wx)})^2 + (PRi(89) - LUT_{PR89(ca,\ cc,wx)})^2 + (\Delta GRi - LUT_{dGR(ca,\ cc,wx)})^2$$

6. The indices ca, cc, wx where δ is minimal determine the ice concentration (and weather index), i.e.:

$$C_T = C_{A\min\delta} + C_{C\min\delta} \quad (8)$$

2.2.2 Land Spillover Correction

Although a land mask is applied to the ice concentration maps, land spillover still leads to erroneous ice concentrations along the coast lines adjacent to open water. This makes operational usage of these maps cumbersome. Therefore, we apply a land spillover correction scheme on the maps. The difficulty is to delete all clearly erroneous ice

concentration while at the same time preserving actual ice concentrations, as for example, along the margins of coastal polynyas. We apply a five step procedure:

1. Classify all pixels of the polar-stereographic grid with respect to the distance to coast. Ocean pixels directly along the coast are classified by 1, whereas pixels farther away are 2 and 3. Open ocean pixels are zero. Land pixels directly along the coast are classified as 4 and pixels farther away have increasing values.

2. All pixels with classes 1 or 2 will be assessed for erroneous sea ice concentrations due to land spillover by analyzing the 7 by 7 pixel neighborhood. The area of the neighborhood (7 pixels or 87.5 km) needs to be greater than the AMSR-E antenna pattern. Pixels with values of 3 and 0 will not be changed.

3. Check whether all class 3 pixels in 7 pixel neighborhood are open water (if so, set ice concentration to 0).

4. Calculate an average sea ice concentration for the 7 by 7 pixel box assuming all ocean pixels have zero ice concentration and all land pixels have an ice concentration of 90%. This approximates a theoretical concentration caused by land spillover only.

5. If the AMSR-E ice concentration is less than or equal to this value, set pixel at center of box to open water.

Figure 4 shows an example ice concentration with and without the land spillover correction.

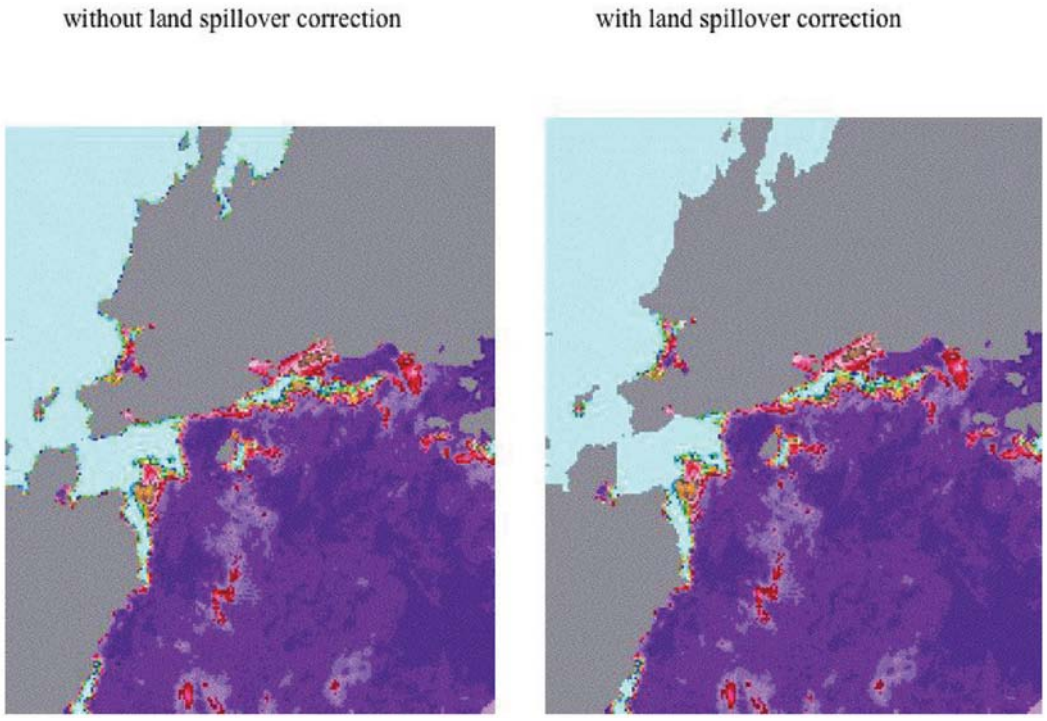

Figure 4 Map of ice concentration with and without land spillover correction.

2.2.3 Reduction of Atmospheric Effects

The NT2 algorithm has an atmospheric correction scheme as an inherent part of the algorithm. It provides weather-corrected sea ice concentrations through the utilization of a forward atmospheric radiative transfer (RT) model. However, to eliminate remaining severe weather effects over open ocean, two weather filters based on the spectral gradient ratio are implemented using threshold values similar to those used by the NT algorithm [Gloersen and Cavalieri, 1986; Cavalieri et al., 1995]. However, the advantage of the RT atmospheric correction is that not only are spurious ice concentrations over the open ocean removed, but atmospheric corrections are applied to ice covered portions of the ocean.

Figure 5 shows AMSR-E sea ice concentration maps for the Sea of Okhotsk. Figure 5a shows the ice concentration map if PR_R (19), PR_R (89), and ΔGR are used without any weather correction. Figure 5b shows the ice concentration map with the NT2 weather correction. The differences between Figure 5a and 5b are shown in Figure 5d and illustrate the effect of the weather correction not only over the open ocean, but also over the sea ice. More severe weather effects over the open ocean (for example, in the bottom right corner) are finally removed by the NT weather filters (Figure 5c). The threshold for the GR(37V19V) NT weather filter (Gloersen and Cavalieri, 1986) is 0.05, where the threshold for the GR(22V19V) NT weather filter (Cavalieri et al., 1995) is 0.045. If the respective GR values exceed these thresholds, the sea ice concentrations are set to zero. Figure 5e shows the difference in ice concentrations between the retrievals using only the NT2 weather correction and the retrievals using both the NT2 correction and the NT filters. A slight change along the ice edge is observed.

Even with both the atmospheric correction scheme and the GR filters, we still had problems with residual weather contamination particularly at low latitudes. A filter based on monthly climatological sea surface temperatures (SSTs) from the National Oceanic and Atmospheric Administration (NOAA) ocean atlas, used earlier by Cavalieri et al. (1999), was employed to eliminate these low-latitude spurious ice concentrations. In the Northern Hemisphere, any pixel where the monthly SST is greater than 278 K, the ice concentration is set to zero throughout the month; whereas in the Southern Hemisphere, wherever the monthly SST is greater than 275 K, the ice concentration is set to zero throughout the month. The higher SST threshold value in the Northern Hemisphere is needed because the 275 K isotherm used in the Southern Hemisphere is too close to the ice edge in the north. The closest distance the threshold isotherms are to the ice edge is more than 400 km [Cavalieri et al., 1999].

In summary, the order of processing is as follows:

1. Calculate sea ice concentrations with atmospheric correction.
2. Apply GR filters.

3. Apply SST mask.
4. Apply land spillover correction.

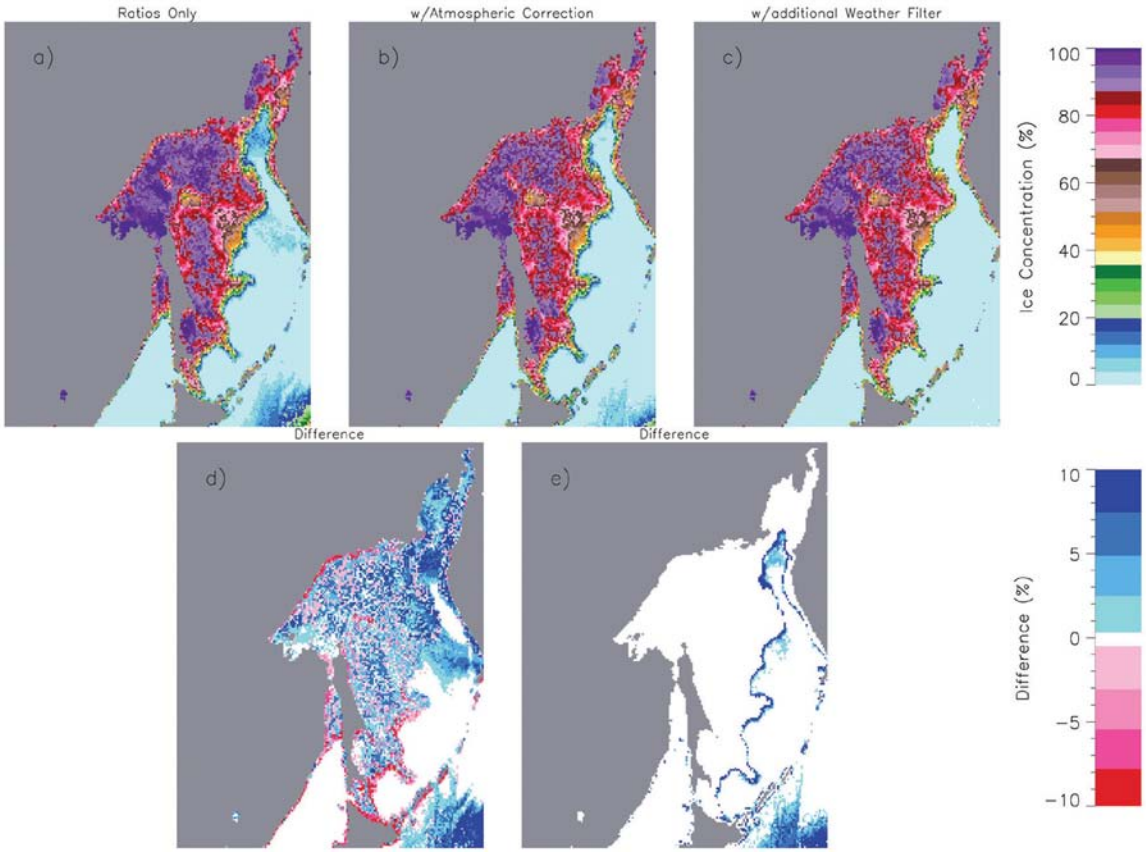

Figure 5 AMSR-E sea ice concentrations for March 1, 2007. (a) Ice concentrations calculated using PR_R (19), PR_R (89), and ΔGR without applying an atmospheric correction; (b) ice concentration with atmospheric correction; (c) final ice concentration with additional clean-up over the open ocean by applying the standard NASA Team GR weather filters; (d) difference between (a) and (b); (e) difference between (b) and (c). Differences greater than 10% have been truncated for the erroneous sea ice concentrations in the lower right corner.

3. Snow Depth on Sea Ice

3.1 Algorithm Theoretical Basis

The AMSR-E snow-depth-on-sea-ice algorithm was developed using DMSP SSM/I data (Markus and Cavalieri, 1998) to estimate snow depth on sea ice from space. The snow depth on sea ice is calculated using the spectral gradient ratio of the 18.7 GHz and 37 GHz vertical polarization channels,

$h_s = a_1 + a_2$ GRV(ice)

where hs is the snow depth in meters, and a_1=2.9 and a_2=-782 are coefficients derived from the linear regression of *in situ* snow depth measurements on microwave data. GRV(ice) is the spectral gradient ratio corrected for the sea ice concentration, C, as follows:

$$GRV(ice) = [T_B(37V)-T_B(19V)-k_1(1-C)] \ / \ [T_B(37V)+T_B(19V)-k_2(1-C)]$$

with $k_1=T_{BO}(37V)-T_{BO}(19V)$ and $k_2=T_{BO}(37V)+T_{BO}(19V)$. The open water brightness temperatures, T_{BO}, are average values from open ocean areas and are used as constants. The principal idea of the algorithm is similar to the AMSR-E snow-on-land algorithm (Kelly et al., 2003) utilizing the assumptions that scattering increases with increasing snow depth and that the scattering efficiency is greater at 37 GHz than at 19 GHz. For snow-free sea ice, the gradient ratio is close to zero and it becomes more and more negative as the snow depth (and grain size) increases. The correlation of regional *in situ* snow depth distributions and satellite-derived snow depth distributions is 0.81 (Figure 6). The upper limit for snow depth retrievals is 50 cm which is a result of the limited penetration depth a 19 and 37 GHz.

3.2 Implementation

The algorithm is applicable to dry snow conditions only. At the onset of melt, the emissivity of both the 19 GHz and the 37 GHz channels approach unity (that of a blackbody) and the gradient ratio approaches zero initially before becoming positive. Thus, snow depth is indeterminate under wet snow conditions. Snow, which is wet during the day, frequently refreezes during the night. This refreezing results in very large grain sizes (Colbeck, 1982) which leads to a reduced emissivity at 37 GHz relative to 19 GHz thereby decreasing GRV(ice) and thus leads to an overestimate of snow depth. These thaw-freeze events, therefore, cause large temporal variations in the snow depth retrievals. This temporal information is used in the algorithm to flag the snow depths as unretrievable from those periods with large fluctuations.

As grain size *in situ* measurements are even less frequently collected than snow depth measurements, the influence of grain size variations could not be incorporated into the algorithm. Because of the uncertainties in grain size and density variations as well as sporadic weather effects, AMSR-E snow depth products will be 5-day averages similar to the snow-on-land product.

Snow depths are retrieved for the entire Southern Ocean, but only for the seasonal sea ice zones in the Arctic, because the microwave signature of snow is very similar to the multiyear ice signature so that snow depth on multiyear ice cannot be retrieved unambiguously. To this end, we use a dynamic multiyear ice mask based on a threshold in GR which evolves on a day-to-day basis starting from October 1 of each year until the onset of melt.

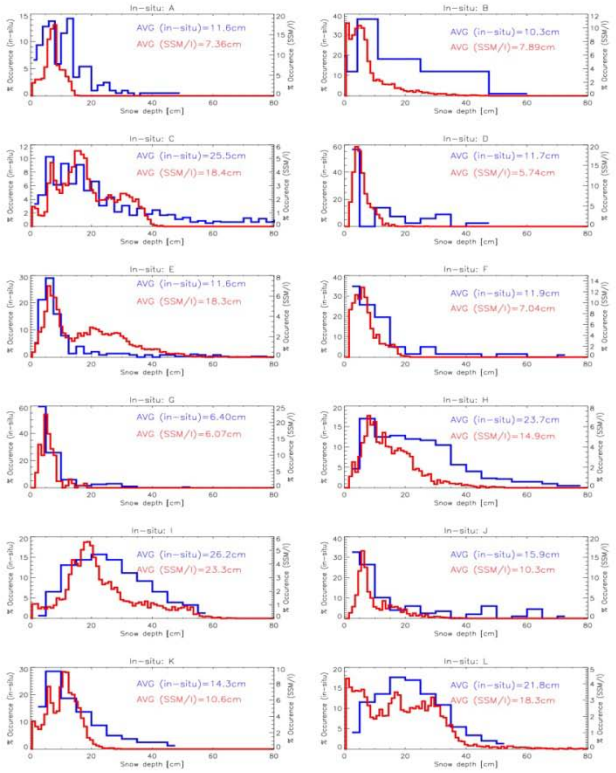

A: **Weddell Sea** **7/86 - 9/86**
(Wadhams et al., 1986)
B: **East Antarctic** **10/88 - 12/88**
(Allison et al., 1993)
C: **Weddell Sea** **9/89 - 10/89**
(Eicken et al., 19994)
D: **East Antartic** **11/91**
(Worby and Massom, 1991)
E: **Weddell Sea** **6/92 - 7/92**
(Drinkwater and Haas, 1994)
F: **East Antarctic** **10/92 - 11/92**
(Worby and Massom, 1995)
G: **East Antarctic** **3/93 - 5/93**
(Worby and Massom, 1995)
H: **Bellingshausen** **8/93 - 9/93**
(Worby et al., 1996)
I: **Amundsen** **9/94 - 10/94**
(Sturm et al., 1998)
J: **East Antarctic** **9/94 - 10/94**
(Jeffries et al., 1995)
K: **Ross Sea** **5/95 - 6/95**
(Sturm et al.,1998)
L: **Ross Sea/Bellingshausen 8/95-9/95**
(Sturm et al., 1998)

Figure 6: Comparison of *in-situ* and SSM/I-derived snow depth distributions [from Markus and Cavalieri, 1998].

4. Sea Ice Drift

4.1 Algorithm Theoretical Basis

The sea ice drift algorithm applies a wavelet transform to the 89 GHz Horizontal (H) channel of the AMSR-E L3 6.25 km brightness temperature map gridded at a resolution of 6.25 km for ice feature detection. These ice features are tracked from day-to-day providing sea ice speed and direction at grid points mapped every 100 km. The algorithm, originally developed at Goddard Space Flight Center (GSFC) for use with DMSP SSM/I imagery, is described by Liu and Cavalieri (1998). The algorithm provides sea ice drift for 5-day periods for both the Arctic and the Antarctic.

The following has been adapted from Liu and Cavalieri (1998) and describes the derivation techniques:

The wavelet transforms of satellite images can be used for near-real-time quick-look analyses of satellite data for feature detection, for data reduction using a binary image, and image enhancement by edge linking. In general, the continuous wavelet transform, Ws (a, b), of a function, s (r), where r = (x, y), is expressed in terms of the complex valued wavelet function, w(r), as follows:

$$W_s(a,\boldsymbol{b}) = \frac{1}{\sqrt{a}} \int s(\boldsymbol{r}) w^* \left(\frac{\boldsymbol{r} - \boldsymbol{b}}{a} \right) d\boldsymbol{r}$$

in which the wavelet function is dilated by a factor a, and shifted by b. The function w(r) is the basic wavelet (Combes et al. 1989). The superscript * indicates complex conjugate. For data analysis, the wavelets frequently used are: a Gaussian modulated sine and cosine wave packet, known as the Morlet wavelet; and the second derivative of a Gaussian, often referred to as the Mexican hat.

4.2 Implementation

To determine drift vectors only over sea ice, not open water, a sea ice mask is used within the sea ice drift algorithm code. Derived from the 18 GHz and 37 GHz Vertical (V) channels of the AMSR-E L3 12.5 km brightness temperature product, the mask approximates sea ice coverage in order to mask out unused vector points.

- Closed contours (those with no other features crossing them, called zero-crossing contours) correspond to the boundary of ice features. Yet these zero-crossing contours may contain many different ice features. To associate a single closed contour with an isolated ice feature, a five percent threshold above the minimum of the wavelet transform is applied as the contour value.
- Next, each closed contour is framed in a rectangular window with its four sides just tangent to the four extreme locations of the closed contour. Each window at a given starting date is used as a template to be matched. The template window is not fixed in size, but is determined by the ice feature at a particular location.
- With the template defined, the templates are then matched with the results from the wavelet transform of the AMSR-E image four days later. Because of the 6.25 km resolution of the AMSR-E image, the displacement of the ice feature may move just a pixel or two in several days. Thus, the domain of the template matching can be restricted to an area with a few pixels (such as 20 pixels) larger than the template window. The matching is done by shifting the template over each pixel in the domain.
- For each location, the absolute values of the differences between the shifted template values and the target values are then summed.
- The sequence of the summation values is then used as a metric of the degree of match of the ice feature. Its minimum indicates a possible match of two displaced ice features. Once the shapes have been matched, the velocity vector can be easily estimated from dividing the relative displacement over a time interval of four days.

Note that the method of template matching outlined above uses a template window determined by the threshold of the wavelet transform of AMSR-E images. This method of template matching of ice features is very efficient, as the only computations involved are logical operations, addition, and subtraction. Furthermore, it is only necessary to match the template pattern to a limited number of target patterns generated by the results of the wavelet transform, not to every location in the image as with classical template

matching. Note also that although template correlation is applied here only to find the translation of the target pattern with respect to the template pattern, it can be extended to find the rotation of the target pattern by incremental rotation of the target pattern in direction and then matching the extent of their agreement (Liu and Cavalieri 1998).

In summary, once a sea ice feature is identified, it is tracked from day-to-day over 4 days. The total displacement over this period then is used to calculate the 5-day sea ice drift (speed and direction). The sea ice speed is given in centimeters per second (cm/s) and direction is given in radians from the horizontal axis of the grid counterclockwise. Zhao and Liu (2007) have compared the AMSR-E sea ice drift with Arctic Ocean buoy data and obtained an RMS error of 3.1 cm/s for the AMSR-E sea ice speed and an RMS error of 26.4 degrees for the AMSR-E sea ice direction.

5. References

Cavalieri, D. J., A microwave technique for mapping thin sea ice, *J. Geophys. Res.*, 99, 12,561-12,572, 1994.

Cavalieri, D.J., P. Gloersen, and W.J. Campbell, Determination of sea ice parameters with the NIMBUS 7 scanning multichannel microwave radiometer, J. Geophys. Res., 89, 5355-5369, 1984.

Cavalieri, D. J., K. St. Germain and C. T. Swift, Reduction of Weather Effects in the Calculation of Sea Ice Concentration with the DMSP SSM/I, *J. Glaciology*, 41, 455-464, 1995.

Cavalieri, D. J., C. L. Parkinson, P. Gloersen, J. C. Comiso, and H. J. Zwally, Deriving Long-Term Time Series of Sea Ice Cover from Satellite Passive-Microwave Multisensor Data Sets, *J. Geophys. Res.*, 104, 15,803-15,814, 1999.

Colbeck, S.C., An overview of seasonal snow metamorphism", *Rev. Geophys. Space Phys.*, Vol. 20, pp. 45-61, 1982.

Combes, J. M., Grossmann, A., and Tchamitchian, Ph., Wavelet: time frequency methods and phase space. *Proceedings of the International Conference on Wavelet, Marseille, France* (New York: Springer-Verlag), 331 pp, 1989.

Comiso, J. C., D. J. Cavalieri, C. L. Parkinson, and P. Gloersen, Passive microwave algorithms for sea ice concentration - A comparison of t wo techniques, Remote Sens. Environ., 60, 357-384, 1997.

Eppler, D.T., and 14 others, Passive microwave signatures of sea ice, in Microwave Remote Sensing of Ice, Geophys. Monogr. Ser., vol. 68, edited by F. Carsey, pp. 47-71, AGU, Washington, D.C., 1992.

Fraser R.S., Gaut, N.E., Reifenstein, E.C., and H. Sievering, Interaction Mechanisms--Within the Atmosphere, in {\it Manual of Remote Sensing}, edited by R.G. Reeves, A.

Anson, D. Landen, pp.181-233, American Society of Photogrammetry, Falls Church, VA, 1975.

Gloersen, P., W. J. Campbell, D. J. Cavalieri, J. C. Comiso, C. L. Parkinson, H. J. Zwally, "Arctic and Antarctic Sea Ice, 1978-1987L Satellite Passive Microwave Observations and Analysis," *NASA Spec. Publ.,* Vol. 511, 290 pp, 1992.

Gloersen, P. and D.J. Cavalieri, Reduction of weather effects in the calculation of sea ice concentration from microwave radiances, J. Geophys. Res., 91, 3913-3919, 1986.

Kelly, R.E., A.T.C. Chang, L. Tsang, and J.L. Foster, A prototype AMSR-E global snow area and snow depth algorithm, IEEE Trans. Geoscience Rem. Sens., 41, 230-242, 2003.

Kummerow, C.,On the accuracy of the Eddington approximation for radiative transfer in the microwave frequencies, J. Geophys. Res., 98, 2757-2765, 1993.

Lubin, D., C. Garrity, R.O. Ramseier, and R.H. Whritner, Total sea ice concentration retrieval from the SSM/I 85.5 GHz channels during the Arctic summer, Rem. Sens. Environ., 62, 63-76, 1997.

Liu, A. K. and D. J. Cavalieri. 1998. On Sea Ice Drift from the Wavelet Analysis of the Defense Meteorological Satellite Program (DMSP) Special Sensor Microwave Imager (SSM/I) Data. *International Journal of Remote Sensing* 19:7, 1415-1423. doi: 10.1080/014311698215522

Markus, T. and D. J. Cavalieri, Snow depth distribution over sea ice in the Southern Ocean from satellite passive microwave data, Antarctic Sea Ice: Physical Processes, Interactions and Variability, Antarctic Research Series, Volume 74, pp 19-39, American Geophysical Union, Washington, DC, 1998.

Markus, T. and D.J. Cavalieri, An enhancement of the NASA Team sea ice algorithm, IEEE Trans. Geoscience Remote Sensing, 38, 1387-1398, 2000.

Markus, T. and D. J. Cavalieri, The AMSR-E NT2 sea ice concentration algorithm: its basis and implementation, *Journal of The Remote Sensing Society of Japan*, Vol. 29, No. 1, 216-225, 2009.

Markus, T. and S.T. Dokken, Evaluation of Arctic late summer passive microwave sea ice retrievals, IEEE Trans. Geoscience Remote Sensing, 40(2), 348-356, 2002 .

Matzler, C., R.O. Ramseier, and E. Svendsen, Polarization effects in sea-ice signatures, IEEE J. Oceanic Eng., OE-9, 333-338, 1984.

Zhao, Y. and A. K. Liu, Arctic Sea-Ice Motion and Its Relation to Pressure Field. *Journal of Oceanography* 63:505-515, 2007.